Secondary Electron Count Imaging in SEM

Akshay Agarwal[a], John Simonaitis[a], Vivek K. Goyal[b], Karl K. Berggren[a]

[a]*Department of Electrical Engineering and Computer Science, Massachusetts Institute of Technology*

[b]*Department of Electrical and Computer Engineering, Boston University*

Abstract

Scanning electron microscopy (SEM) is a versatile technique used to image samples at the nanoscale. Conventional imaging by this technique relies on finding the average intensity of the signal generated on a detector by secondary electrons (SEs) emitted from the sample and is subject to noise due to variations in the voltage signal from the detector. This noise can result in degradation of the SEM image quality for a given imaging dose. SE count imaging, which uses the direct count of SEs detected from the sample instead of the average signal intensity, would overcome this limitation and lead to improvement in SEM image quality. In this paper, we implement an SE count imaging scheme by synchronously outcoupling the detector and beam scan signals from the microscope and using custom code to count detected SEs. We demonstrate a ∼30% increase in the image signal-to-noise-ratio due to SE counting compared to conventional imaging. The only external hardware requirement for this imaging scheme is an oscilloscope fast enough to accurately sample the detector signal for SE counting, making the scheme easily implementable on any SEM.

Keywords: scanning electron microscopy, secondary electrons, electron counting, signal-to-noise-ratio

1. Introduction

Scanning electron microscopy (SEM) is a powerful imaging modality that is routinely used for nanoscale imaging, analysis, and characterization of a wide variety of samples [1]. In SEM, an electron beam with energy typically between 0.5 and 30 keV raster scans over the sample. The position of the electron beam is controlled by electrostatic scan coils, which drive the beam in the horizontal (fast) direction and the vertical (slow) direction. At each scan position (referred to as a pixel), the incident beam causes emission of electrons from the surface of the sample. These secondary electrons (SEs) are detected by an SE detector, which converts the SE intensity from each pixel to a voltage signal. Conventionally, the analog average of this voltage signal is converted to an 8-bit brightness value for each pixel to generate the sample image.

SE count imaging is an alternative SEM imaging scheme in which the analog average of the SE signal intensity would be replaced by the direct count of SEs per pixel. Such an imaging scheme has the potential to provide higher image quality than conventional SE imaging for a given dose of incident electrons [2]. Counting SEs from each pixel would eliminate noise in the image arising from variations in the voltage signal generated by the SE detector and subsequent processing steps. Therefore, an SE count imaging scheme would be beneficial for all types of SE imaging, particularly the imaging of radiation-sensitive samples such as proteins and biomolecules where the imaging dose restricts the achievable image quality [3, 4].

SE count imaging in SEMs was pioneered by Yamada and co-workers [5, 6, 7, 8, 9]. In their work, the SE detector signal was coupled to external discriminator and pulse-counter circuits to count the number of SEs for each scan position on the sample. The collection, processing, and readout of pulses in this circuit was synchronized with the SEM scan position at each pixel. This setup was used to generate SE count images of different types of organic and inorganic samples and to demonstrate an improvement in signal-to-noise-ratio (SNR) for digital imaging compared to conventional imaging. However, this implementation did not lead to SE counting being incorporated into commercial SEM imaging. An important factor responsible for the unavailability of SE count imaging was the external circuitry required for counting SEs and synchronizing the counting with the SEM scan coils. Developing these external circuits and making them compatible with different SEM hardware and software can be a challenge. Furthermore, the requirement for synchronizing electronics also limited this experiment to long pixel dwell times (typically tens of µs). More recently, SE image histograms have been investigated for counting SEs [2, 10], motivated in part by similar work in scanning transmission electron microscopy (STEM) [11, 12, 13, 14]. However, such techniques are limited by the same voltage signal variations that are present in conventional SE imaging. Therefore, an accurate SE counting method that does not require external circuits and nanosecond-scale synchronization is of interest and would enable more widespread adoption of SE count imaging.

In this work, we will demonstrate an SE count imaging scheme by synchronously outcoupling the SE detector and SEM beam scan signals onto an oscilloscope, and processing the outcoupled data using custom MATLAB code to count the number of SEs detected for each sample pixel. Using this technique, we imaged a copper mesh sample and demonstrated a $\sim$30% increase in the image signal-to-noise-ratio for SE count imaging compared to conventional SEM imaging. The only external hardware requirement to implement this scheme was an oscilloscope; we did not use any ns-scale synchronization circuits unlike previous SE count imaging schemes. Therefore, this SE count imaging scheme could potentially be implemented on many different SEM systems and incorporated with standard SEM software.

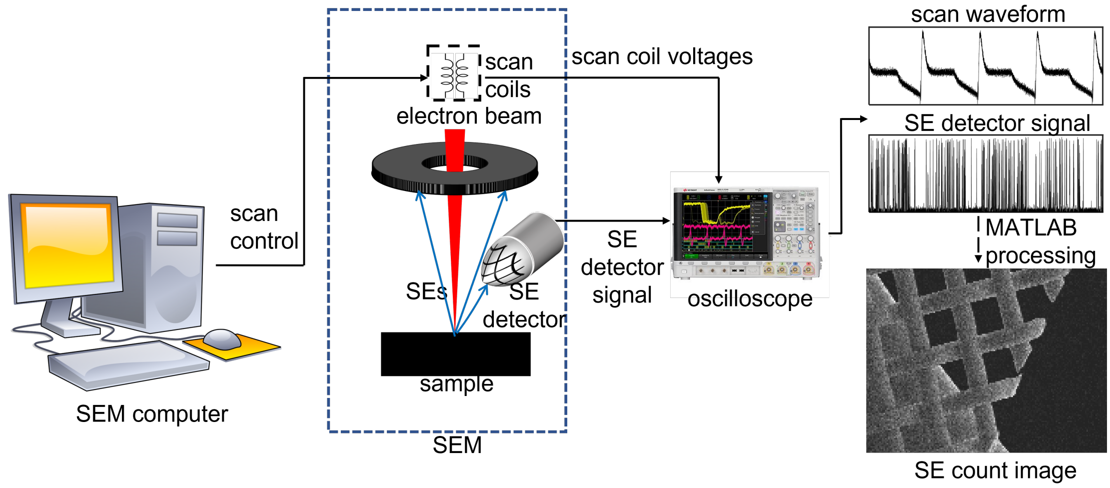

Figure 1: Experimental setup for SE count imaging. The SEM computer controls the scan area and speed on the SEM. We outcoupled both the scan coil voltages and the SE detector signal onto a 2 GHz oscilloscope. Data collection on the oscilloscope was triggered by the sawtooth-shaped scan coil voltage signal. Each acquisition frame consisted of the scan waveform and the SE detector signal with their time axes referenced to the same retrace spike. We collected several such acquisition frames and processed them using custom MATLAB code to generate the final SE count image.

2. Experimental Methods

In this section we will describe the experimental setup as well as the processing steps we took to obtain SE count images. We used a Zeiss LEO 1525 SEM for all the results reported in this paper. We will refer to the SEM scan voltage that scans the beam horizontally across the sample as the *horizontal linescan waveform*. An image is computed from the SE detector signal recorded for a series of such horizontal linescan waveforms. We will refer to the horizontal linescan waveform and the SE detector signal collected during one scan over the sample area being imaged as an *acquisition frame*.

2.1. Imaging setup

Figure 1 is a schematic of our SE count imaging setup. As is usually done in SEM, we used the SEM computer to control beam scan parameters such as scan speed and scan area (*i.e.*, magnification). The SEM we used was equipped with two SE detectors – an in-chamber detector and an in-lens detector. We outcoupled the signal from both SE detectors as well as the SEM scan coil voltage waveforms to three channels of an oscilloscope (2 GHz LeCroy WaveRunner 6200A) using BNC cables. This outcoupling allowed us to read out full acquisition frames from the SEM. The linescan waveform consists of three regions: (1) the trace, during which the voltage is ramped and the electron beam scans across the sample, (2) the retrace spike, when the electron beam is moved back to the start of the line, and (3) a short rest period before the beam starts scanning again. We discuss features of the scan waveform in more detail in Section S1 of the Supplementary Information.

We configured the collection of an acquisition frame on the oscilloscope to be triggered by the retrace spike of the first horizontal linescan voltage waveform in the frame. This trigger voltage setting provided a common time axis for both the linescan waveform and the SE detector signal within an acquisition frame. There was some variation in the exact time at which signal collection was triggered due to noise in the linescan signal, which led to misalignment between successive acquisition frames. In Section 2.3 we will discuss how this variation affected the data we collected and how we corrected for it in the MATLAB code.

We specified the data collection time for an acquisition frame on the oscilloscope to be a few ms longer than the total scan time for the area we were imaging to ensure that the entire scan area was contained in each acquisition frame. The typical acquisition frames we collected had a pixel resolution of around 200×200 pixels, and we used a pixel dwell time of 440 ns for all data acquisition. Therefore, the data collection time for each acquisition frame was on the order of 20 ms. We found an oscilloscope sampling time of 10 ns to be adequate for sampling the SE detector signal pulses. Therefore, any oscilloscope with a sampling frequency over 100 MHz could be used to collect acquisition frames. Over a total collection time of 20 ms, the sampling rate of 10 ns corresponded to 2×10^6 signal samples. This number is close to the maximum number of samples that could be stored on our oscilloscope at a time. This limitation in the maximum number of samples per acquisition frame limited the pixel resolution of the images we could capture.

We collected 32 acquisition frames from the same scan area on both the in-chamber and in-lens SE detectors to construct SE count images of that area, at a beam current of 2.3 pA and a pixel dwell time of 440 ns. We had found the detective quantum efficiency (DQE) [15, 2] of the in-chamber detector to be 0.16 and that of the in-lens detector to be 0.32 previously [10], for the working distance used in this work. To generate SE count images, we added the SE counts obtained from these two detectors. We note that saving the data corresponding to each acquisition frame on the oscilloscope took several seconds. We manually blanked the incident electron beam during this time to minimize sample exposure between acquisition frames.

As discussed earlier, the acquisition frames we collected contained the SEM linescan as well as the SE detector signal referenced to a common time axis. In the rest of this section, we will present an analysis of the SE detector signal to establish that it can be used to count SEs, and then discuss the MATLAB code we used to generate SE count images from acquisition frames. Section 2.2 shows an analysis of the SE detector signal. In the MATLAB code we addressed several challenges in order to generate SE count images. First, we needed to account for slight variations in the triggering time on the oscilloscope due to noise in the linescan waveform, which we will describe in Section 2.3. Second, we needed to extract the section of the SE detector signal that corresponded to the trace section of the linescan where the incident beam was actually scanning over the sample. We will describe this extraction in

Section 2.4. With these challenges addressed, we counted the number of SE pulses for every pixel in each acquisition frame. We will describe our counting algorithm in Section 2.5.

2.2. Analysis of SE detector signal

Figure2_v4.png

Figure 2: Statistics of SE detector signal. (a) 5 µs output signal from the in-chamber detector on the oscilloscope (sampled at 10 ns) showing pulses due to detected SEs. (b) Histogram of signal pulse heights showing that most pulses are saturated at 5.6 V. (c) Histograms of the FWHM pulse durations for beam current I between 1.1 pA and 5.4 pA. All histograms have a mean of 180 ns. (d) Distribution of inter-arrival times of SE pulses on the in-chamber detector. Measured values are displayed as blue unfilled circles. The orange line is an exponential fit with a parameter of 0.47/µs. This fit parameter is close to the expected SE count rate of 0.45 SEs/µs, as discussed in the text.

Figure 2(a) shows a 5 µs snapshot of the in-chamber SE detector signal, showing voltage pulses from incident SEs. We collected this data at an incident beam current of 2.3 pA and a pixel dwell time of 440 ns, scanning over a homogeneous sample made of aluminum. In previous work, we had found that an imaging current of 2.3 pA was well within the linear response region of our SE detectors and had also described the statistics of these voltage pulses [10]. We had concluded that each pulse corresponds to one detected SE, thereby allowing the counting of SEs. Here, we reiterate the measurements which led to this conclusion.

At the beam current of 2.3 pA used in our experiments, assuming that the sample SE yield is 0.2 [16] and the detector DQE is 0.16, the mean rate of SEs incident on the detector should be 0.45/µs. An analysis of the image histogram statistics confirms this mean SE rate, as described in Section S2 of the Supplementary Information. Therefore, assuming that the probability distribution function for the number of SEs detected per pixel is roughly Poissonian, the probability of getting multiple SEs during one pixel dwell time is $\sim 1.7\%$ [17, 18]. Furthermore, the low SE yield results in the probability of one incident beam electron emitting multiple SEs being low ($<2\%$), further indicating that each detected voltage pulse comes from at most one SE.

Analysis of the width statistics of these voltage pulses presented more evidence for our conclusion. The image brightness and contrast settings we used resulted in most pulses having a maximum voltage around 5.6 V, as can be seen in the pulse height distribution plotted in Figure 2(b). This saturated height distribution was advantageous while counting pulses, as described in Section 2.5. Figure 2(c) shows the distribution of the full-width-at-half-maximum (FWHM) width of these pulses at different values of the beam current from 1.1 pA to 5.4 pA. We observed the pulse width distribution remained unchanged as the current increased, indicating that each pulse corresponds to one SE. The mean

Figure3_v4.png

Figure 3: Acquisition frame alignment and SE pulse extraction. (a) Linescans from two acquisition frames at a pixel dwell time of 440 ns. The top linescan (orange) is misaligned with the bottom linescan (blue) by one line. We added a vertical offset of 1.1 V to the orange linescan for ease of viewing. (b) Cross-correlation of the two linescans in (a). The offset between zero delay (indicated by the dashed black line) and the highest cross-correlation peak (indicated by the dotted red line) equals the misalignment of 118.4 µs between the two linescans. (c) Extraction of useful SE signal, *i.e.*, the sections of the raw SE signal (yellow) corresponding to the trace section of the linescans, during which the incident beam scans over the sample (orange). We added a vertical offset of 6 V to the raw SE detector signal for ease of viewing. (d) Counting SE pulses. The dotted black square waveform shows successive image pixels, with even pixels assigned a value of 0 and odd pixels a value of 5. The first of the SE pulses (solid black) is within an odd pixel. However, although the second pulse originates in an even pixel, most of its intensity is present in the next (odd) pixel.

FWHM pulse width was about 180 ns. Based on this mean FWHM pulse width, we used an oscilloscope sampling time of 10 ns for all acquisition frames in our experiments.

Further evidence is provided in Figure 2(d), which shows the distribution of pulse inter-arrival times. These inter-arrival times were measured as the time duration between the instants when two successive pulses reached half their maximum values. The inter-arrival times for a process following a Poisson distribution with mean λ are expected to obey an exponential distribution given by $\lambda e^{-\lambda t}$. As can be seen in the figure, the inter-arrival time distribution is indeed well-fitted by an exponential distribution for inter-arrival times greater that $\sim$1 µs. The decay rate λ for this exponential distribution is 0.47/µs. This rate is very close to the expected SE detection rate calculated earlier (0.45/µs), which again shows that each voltage pulse corresponds to one detected SE. We believe that the deviation between the observed pulse inter-arrival times distribution and the exponential fit below 1 µs was a result of limitations in the speed of the scintillator and signal processing electronics in the SE detector.

Having described the evidence for the each of the voltage pulses arising from individual SEs, we will now describe features of our MATLAB code to generate SE count images from the collected acquisition frames.

2.3. Aligning acquisition frames and finding linescan period

A major challenge we addressed in the MATLAB code for SE count imaging was temporal alignment of all the acquisition frames. Figure 3(a) shows the linescan waveforms for the first few lines for the first (orange curve) and second (blue curve) acquisition frames captured on the oscilloscope during one imaging experiment. Note that in this figure we added a vertical voltage offset to the scan waveform for the first acquisition frame for ease of viewing. We can see that the two frames were misaligned by a time duration corresponding to one linescan. As we had discussed in Section 2, we set the trigger level on the oscilloscope to be close to the peak voltage of the spike that followed each linescan (this spike can be seen at the end of each of the voltage ramps, which correspond to the horizontal scan, in Figure 3. The misalignment in Figure 3(a) was caused by noise in the linescan waveform. This noise caused the exact trigger level to be first reached on different spikes for different frames. Each acquisition frame still had SE detector signal and scan waveform referenced to the same time axis, but the misalignment caused the time axis to differ for different frames. We ensured that this misalignment between frames was small enough that the signal from the whole image frame was still captured in the acquisition frame on the oscilloscope.

In the SE count imaging code, we decided to use the linescan waveform for the first frame as the absolute reference to measure the misalignment of all other frames. We used the one-dimensional cross-correlation between the linescans for first frame and those for each of the succeeding frames to measure the misalignment between that frame and the first frame. Figure 3(b) is the cross-correlation between the linescans for the two acquisition frames from Figure 3(a). The cross-correlation of two input signals is the product of the two signals as a function of a delay introduced in one of the signals. As the delay changes, one signal 'slides over' the other, and the cross-correlation magnitude depends on how similar the two signals are at that delay. Since the two linescan waveforms were periodic, the cross-correlation showed periodic peaks. Figure 3(b) shows a few of these peaks around zero delay. The highest of these peaks occurred for a delay at which the two linescans were exactly aligned with each other. In Figure 3(b), we have indicated zero delay with a dashed black vertical line. The delay for the highest peak was 118.4 µs, indicated by the dotted red vertical line. The lower bound on the alignment precision of this technique was equal to the oscilloscope sampling time of 10 ns. Using this technique we extracted the misalignment for the linescan in each acquisition frame and delayed or advanced the scan waveform and the SE detector signal for that frame by this misalignment to ensure that all frames were aligned to the same time axis.

An additional advantage of calculating the cross-correlation was that the gap between successive peaks of the autocorrelation gave us the periodicity of the linescan waveform. We averaged the values of the gap between the 20 highest cross-correlation peaks to get the value of the linescan period. This period would have been much more difficult to extract from the waveform directly due to noise on the signal, and the cross-correlation was a much more accurate way to measure the periodicity. For the linescans shown in Figure 3(a), we measured this period to be 118.4 µs. Knowing the pixel dwell time, we also extracted the image resolution from this period. We verified the extracted image resolution by directly analyzing the linescan waveform, as described in Section S3 of the Supplementary Information.

2.4. Finding linescan duration and extracting SE signal during scanning

The final step before counting the number of SE pulses for each image pixel was determining the start and end time of the trace section of each linescan in every acquisition frame. The trace section of the linescan corresponds to the part of the linescan voltage waveform where the voltage is ramped to scan the beam across the sample. This step was important because in addition to the expected signal pulses during the trace section of the linescan, the SE detector also recorded signal pulses during the other sections of the linescan waveform. Figure 3(c) shows the raw signal from the in-chamber SE detector (in yellow) and the scan waveform (in blue). Note that in this figure we added an offset of 6 V to the raw SE signal for ease of viewing. We can see that there are signal pulses during the entire waveform, and not just in the trace (*i.e.* ramp) region of the waveform. These signal pulses originated from the sample material at the rest position of the incident electron beam before it started the next linescan. Since this signal does not correspond to the sample region being imaged, it should not be used to generate the image. By finding the start and end time of the trace sections in all the linescans, we can exclude this signal from our analysis and count only the pulses that were recorded when the beam was scanning. Furthermore, having determined the number of pixels per line as described in the previous section, we can use these start and end times as references to segment the signal from one linescan into pixels.

We found the start and end time of the trace section of first linescan in the first acquisition frame manually. With all the acquisition frames aligned and knowing the period of the linescan waveform (as discussed in the previous section), the MATLAB code automatically determined the start and end times of the trace sections in all other linescans in all frames. Once we had determined these times we could determine which sections of the SE signal were acquired during the trace sections and ignore the rest of the detector signal. Figure 3(c) shows the sections of the in-chamber detector signal acquired during the trace section in red (without any offset). These sections line up with the trace section of the linescan waveform. After extracting these sections, we divided the trace period into pixels using the extracted number of pixels as described in the previous section. With this segmentation done, our code was ready to count the number of pulses in each pixel.

2.5. Counting SE pulses

We generated SE count images by counting the number of SE pulses in each pixel in our code. As described in Section 2.2, we used contrast and brightness settings so that most of the SE pulses were saturated at a voltage of 5.6 V. This saturation enabled us to use a simple threshold in our code to filter out low voltage noise pulses and count SE pulses originating from the sample. In the MATLAB code we set this threshold voltage to be 1 V.

Figure 3(d) shows an example of the in-chamber detector signal pulses (solid black). In this figure, we have also plotted a square waveform corresponding to successive pixels that the code segmented the trace section of the linescan into (dotted black curve), with odd pixel numbers arbitrarily assigned a value of 5 and even pixels a value of 0 for ease of viewing. We can see that the first SE detector pulse originates in one of the odd pixels and is fully contained within it. The SE imaging code counted one SE in that pixel for this frame. There were no SE pulses for the next 6 pixels. The next SE pulse originated close to the end of an even pixel, but most of its intensity was present in the next (odd) pixel. We assigned this pulse to the even pixel it originated in. The conventional imaging scheme used by the SEM computer would have accounted most of its intensity in the next, odd pixel, leading to inaccuracy in the displayed intensity of that pixel. This 'spillover' effect has been discussed in the context of STEM imaging [13] and is one of the reasons we expect SE count images to be more accurate that conventional SEM images.

We found the number of SE counts per pixel for each of the 32 acquisition frames for both the in-lens and in-chamber detectors, and added the counts to obtain the final image. We note that SEMs typically allow the user to "mix" the signal from the two detectors in a desired ratio; our method of adding the counts corresponds to a 50/50 mixing.

3. Results

To demonstrate our SE count imaging technique, we chose a sample consisting of a free-standing copper mesh with a period of 120 µm suspended over vacuum. We chose this sample so that we could compare the quality of the SE count image with the conventional image based on the contrast between the image pixels representing the copper mesh and those representing the background vacuum, as well as easily evaluate the SNR of the image. We used an imaging current of 2.3 pA and a pixel dwell time of 440 ns.

Figure 4(a) is an SE count image of the copper mesh generated using the combined SE signal on the in-chamber and in-lens detectors summed over 32 acquisition frames. The pixel resolution of this image is 262×188. The colorbar in Figure 4(a) indicates the number of SEs for a given pixel greyscale level. The maximum number of SEs for any pixel in the image was 50 (summed over all 32 acquisition frames), and the mean number of SEs per pixel in the image was 5.05.

Figure 4(b) is an image of the same sample generated by finding the average signal for every pixel using the same acquisition frame dataset as Figure 4(a). To obtain this image, we found the average signal level for every pixel across all 32 frames. This image represents a conventional SEM image; we checked that the statistics of this image were close to those of an image of this sample generated by the SEM software. We scaled the pixel intensities in this image so that the mean intensity in this image was equal to the mean SE count in Figure 4(a), *i.e.,* 5.05.

From Figures 4(a) and (b), we can see that the contrast of the copper mesh compared to the background vacuum appears to be lower in the SE count image compared to the conventional image. We numerically evaluated the contrast by dividing the sample into two types of pixels – 'sample' pixels representing the copper mesh and 'background' pixels representing the background vacuum. Next, we found the mean pixel intensity for the sample (I_{sample} and the background $I_{\text{background}}$ for both the SE count and conventional image (for the SE count image, this mean intensity corresponds to the mean number of detected SEs).

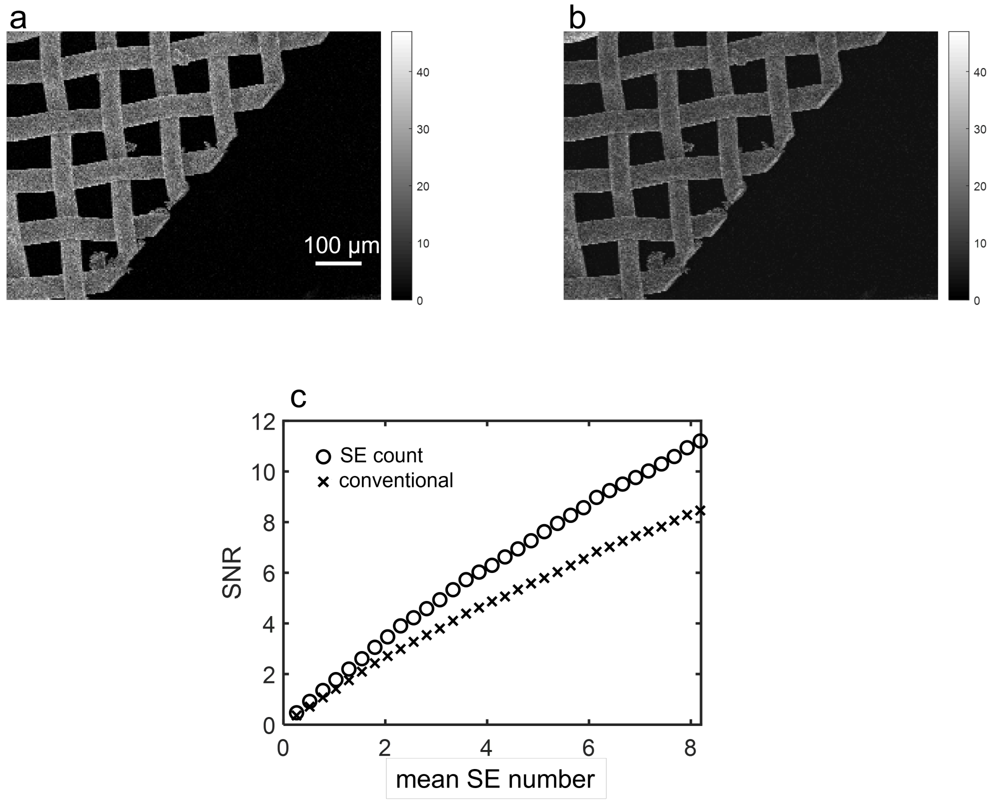

Figure 4: SE count imaging. (a) SE count image of a 120 µm period copper mesh suspended over vacuum. We generated this image by adding the SE counts from the in-chamber and in-lens detectors over all 32 acquisition frames. The frames were collected at an incident beam current of 2.3 pA, energy of 10 keV, and a pixel dwell time of 440 ns. The image pixel resolution is 262×188. The mean SE count in the image is 8.18. (b) Conventional image of the same copper mesh grating under the same imaging conditions and scaled to the same mean pixel intensity as the mean SE count in (a). This image shows lower contrast between the copper mesh and background than (a). (c) SNR (refer text for definition) as a function of the mean SE number for the SE count (unfilled circles) and conventional (crosses) images. The SNR increases with mean SE number for both images and is always $\sim 30\%$ higher for the SE count image. The SNR for the SE count image is also more linear than the SNR for the conventional image.

Finally, we evaluated the contrast K as [19]:

$$K = \frac{I_{\text{sample}} - I_{\text{background}}}{I_{\text{sample}} + I_{\text{background}}}$$

Using this technique, we obtained a contrast of 0.64 for the conventional image and 0.95 for the SE count image, demonstrating the superior image quality for the counting technique.

As a second metric to compare the quality of the SE count and conventional images, we evaluated their SNR using a technique first developed by Thong et al. [20]. We estimated the signal and noise contributions in the SE image by considering the image autocorrelation function. By varying the number of acquisition frames used to compute the final image, we obtained SNR values for both SE count and conventional imaging for different mean SE counts. We describe this method in more detail in Section S4 of the Supplementary Information.

Figure 4(c) is a plot of the SNR for the SE count (unfilled circles) and conventional image (crosses) as a function of the mean SE number. This mean SE number is equal to the mean SE count for the SE count image, and the mean pixel intensity for the conventional image. We can see that for both images the SNR increases as a function of the mean SE number. Furthermore, the SNR for the SE count image is always $\sim$ 30% higher than the SNR for conventional imaging. For example, an SNR of 8 is first achieved for SE count imaging at a mean SE count of 5.38, while for conventional imaging it is achieved at an SE count of 7.68. Since the mean SE count scales linearly with the incident beam current [10], this difference represents an incident electron dose reduction of 30% due to SE count imaging for the same SNR.

4. Conclusions

In this paper, we implemented SE counting using a 32-acquisition-frame dataset that we acquired by synchronizing the collection of SE detector signal and the SEM scan function on an oscilloscope. We developed code to process this raw dataset to generate SE count images. Our implementation of SE count imaging increased image contrast by 48% and SNR by 30% compared to conventional imaging. The major advantage of previous SE counting schemes is that we captured all the fast timing and processing complexity in the SE count imaging code instead of needing to implement it in hardware, which makes our scheme easy to implement on any SEM. Extending our SE scheme to larger acquisition frame sizes, as well as live implementation of the scheme will be the subject of future work. Potential designs for live SE count imaging schemes are discussed in Section S6 of the Supplementary Information.

Our implementation of SE count imaging relies on the observation that each pulse in the SE detector voltage waveform corresponds to one detected SE. This observation allowed us to use imaging conditions that saturated the heights of most voltage pulses, and count the number of voltage pulses per pixel to obtain a count of the number of SEs emitted from that pixel. This observation is critically dependent on the low imaging current (2.3 pA) and sample SE yield (assumed to be 0.2 [16]) in our experiments, as we have already discussed in Section 2.2. In other charged-particle imaging techniques such as helium-ion microscopy (HIM), this observation would no longer be valid, due to the much higher SE yield of such modalities [21, 22]. Each voltage pulse could then correspond to multiple SEs. In this case, correlations between the height of the voltage pulse and the number of SEs that produce it could be used to count SEs, provided that the scintillator and amplifier used in the detector is sufficiently linear.

In addition to imaging, an immediate application of our SE count method is the study of deviations from Poisson behavior in the statistics of SEs [23, 24, 25, 15, 26, 27, 28, 17, 18]. The study of such deviations is important for theoretical modelling of SE emission and imaging. In Section S5 of the Supplementary Information, we present a preliminary analysis of the probability distribution of SE counts obtained from the experiments reported in this paper, and extracted the degree of deviation from Poisson statistics. We found that the variance of the SE count distribution for the pixels containing the copper mesh was larger than the mean SE counts by a factor of 1.4, indicating deviations from ideal Poisson statistics. A related application of our method is the measurement of the sample SE yield, if the DQE of the SE detector has been characterized previously. By imaging a uniform sample of the material and extracting the mean SE counts using our technique, the SE yield can be directly measured.

Acknowledgements

The authors thank Navid Abedzadeh for help with the oscilloscope measurements, and the QEM-2 collaboration for insightful discussions. The authors also acknowledge Minxu Peng, James LeBeau, Dirk Englund, Tony Zhou, Marco Turchetti, and Phillip Keathley for helpful feedback. This work was supported by the Gordon and Betty Moore Foundation. This material is based upon work supported by the U.S. National Science Foundation under Grant No. 181596 and a Graduate Research Fellowship under Grant No. 1745302.

Bibliography

[1] Ludwig Reimer. Introduction. In *Scanning Electron Microscopy*, pages 1–12. Springer-Verlag Berlin Heidelberg New York, 2nd edition, 1998.

[2] David C. Joy. Noise and its effects on the low-voltage SEM. In *Biological Low-Voltage Scanning Electron Microscopy*, pages 129–144. Springer New York, New York, NY, 2007.

[3] R. F. Egerton, P. Li, and M. Malac. Radiation damage in the TEM and SEM. *Micron*, 35(6):399–409, 2004.

[4] R. F. Egerton. Radiation damage to organic and inorganic specimens in the TEM. *Micron*, 119(November 2018):72–87, 2019.
[5] S. Yamada, T. Ito, K. Gouhara, and Y. Uchikawa. Electron counting for secondary electron detection in SEM. *Scanning*, 12(5):I–28 – I–29, 1990.
[6] S. Yamada, T. Ito, K. Gouhara, and Y. Uchikawa. Secondary electron counting images in SEM. In *Proceedings of the XIIth International Congress for Electron Microscopy*, pages 402–403, 1990.
[7] S. Yamada, T. Ito, K. Gouhara, and Y. Uchikawa. Electron-count imaging in SEM. *Scanning*, 13:165–171, 1991.
[8] S. Yamada, T. Ito, K. Gouhara, and Y. Uchikawa. High-speed electron counting system for TV-scan rate SE images of SEM. In *Proceedings of the 49th Annual Meeting of the Electron Microscopy Society of America*, pages 512–513, 1991.
[9] Yoshiki Uchikawa, Kazutoshi Gouhara, Satoru Yamada, Tsutomu Ito, Tetsuji Kodama, and Pooja Sardeshmukh. Comparative study of electron counting and conventional analogue detection of secondary electrons in SEM. *Journal of Electron Microscopy*, 41(4):253–260, 1992.
[10] Akshay Agarwal, John Simonaitis, and Karl K. Berggren. Image-histogram-based secondary electron counting to evaluate detective quantum efficiency in SEM. *Ultramicroscopy*, 224:113238, 2021.
[11] Ryo Ishikawa, Andrew R. Lupini, Scott D. Findlay, and Stephen J. Pennycook. Quantitative Annular Dark Field Electron Microscopy Using Single Electron Signals. *Microscopy and Microanalysis*, 20(01):99–110, 2014.
[12] Xiahan Sang and James M Lebeau. Characterizing the response of a scintillator-based detector to single electrons. *Ultramicroscopy*, 161:3–9, 2016.
[13] Andreas Mittelberger, Christian Kramberger, and Jannik C. Meyer. Software electron counting for low-dose scanning transmission electron microscopy. *Ultramicroscopy*, 188:1–7, 2018.
[14] Tiarnan Mullarkey, Clive Downing, and Lewys Jones. Development of a practicable digital pulse readout for dark-field stem. *Microscopy and Microanalysis*, page 1–10, 2020.
[15] C. W. Oatley. The detective quantum efficiency of the scintillator/ photomultiplier in the scanning electron microscope. *Journal of Microscopy*, 139(2):153–166, 1985.
[16] H. Seiler. Secondary electron emission in the scanning electron microscope. *Journal of Applied Physics*, 54(11):R1, 1983.
[17] Luděk Frank. Noise in secondary electron emission : the low yield case. *Journal of Electron Microscopy*, 54(4):361–365, 2005.
[18] Makoto Sakakibara, Makoto Suzuki, Kenji Tanimoto, Yasunari Sohda, Daisuke Bizen, and Koji Nakamae. Impact of secondary electron emission noise in SEM. *Microscopy*, 68(4):279–288, 2019.
[19] Glenn D. Boreman. Modulation Transfer Function. In *Modulation Transfer Function in Optical and Electro-Optical Systems*, pages 85–107. SPIE, 1000 20th Street, Bellingham, WA 98227-0010 USA, 2001.
[20] J. T. L. Thong, K. S. Sim, and J. C. H. Phang. Single-image signal-to-noise ratio estimation. *Scanning*, 23(5):328–336, 2001.
[21] J Notte, R Hill, S McVey, L Farkas, R Percival, and B Ward. An introduction to helium ion microscopy. *Microscopy and Microanalysis*, 12(S02):126–127, 2006.
[22] Takuya Yamanaka, Kensuke Inai, Kaoru Ohya, and Tohru Ishitani. Simulation of secondary electron emission in helium ion microscope for overcut and undercut line-edge patterns. In John A. Allgair and Christopher J. Raymond, editors, *Metrology, Inspection, and Process Control for Microlithography XXIII*, volume 7272, pages 799 – 807. International Society for Optics and Photonics, SPIE, 2009.
[23] Bernhard Kurrelmeyer and Lucy J Hayner. Shot Effect of Secondary Electrons from Nickel and Beryllium. *Physical Review*, 52(1937):952–958, 1937.
[24] T. E. Everhart, O. O. Wells, and C. W. Oatley. Factors affecting contrast and resolution in the scanning electron microscope. *Journal of Electronics and Control*, 7(2):97–111, 1959.
[25] C. W. Oatley. Detectors for the scanning electron microscope. *Journal of Physics E: Scientific Instruments*, 14:971–976, 1981.
[26] W. Baumann, A. Niemietz, L. Reimer, and B. Volbert. Noise measurements of different SEM detectors. *Electron Microscopy 1980*, 3:174–175, 1980.

[27] W. Baumann and L. Reimer. Comparison of the Noise of Different Electron Detection Systems Using a Scintillator-Photomultiplier Combination. *Scanning*, 4:141–151, 1981.

[28] L. Novak and I. Müllerova. Single electron response of the scintillator-light guide-photomultiplier detector. *Journal of Microscopy*, 233(1):76–83, 2009.